In-situ Measurements and Thermo-mechanical Simulation

of Ti-6Al-4V Laser Solid Forming Processes

Xufei Lu[a,b], Xin Lin[a,b,*], Michele Chiumenti[c,**], Miguel Cervera[c],

Yunlong Hu[a,b], Xianglin Ji[a], Liang Ma[a,b], Weidong Huang[a,b]

[a] *State Key Laboratory of Solidification Processing, Northwestern Polytechnical University, Youyixilu, Xi'an, Shaan Xi 710072, P. R. China*

[b] *Key Laboratory of Metal High Performance Additive Manufacturing and Innovative Design, MIIT China, Northwestern Polytechnical University, Youyixilu, Xi'an, Shaan Xi 710072, P. R. China*

[c] *International Center for Numerical Methods in Engineering (CIMNE), Universidad Politécnica de Cataluña (UPC), Edificio C1, Campus Norte, Gran Capitán s/n, 08034 Barcelona, Spain*

Abstract: Residual stresses and distortions are two technical obstacles for popularizing the Additive Manufacturing (AM) technology. The evolution of the stresses in AM components during the thermal cycles of the metal depositing process is not yet clear, and more accurate in-situ measurements are necessary to calibrate and validate the numerical tools developed for its simulation. In this work a fully coupled thermo-mechanical analysis to simulate the Laser Solid Forming (LSF) process is carried out. At the same time, an exhaustive experimental campaign is launched to measure the temperature evolution at different locations, as well as the distortions and both the stress and strain fields. The thermal and mechanical responses of single-wall coupons under different process parameters are recorded and compared with the numerical models. Good agreement between the numerical results and the experimental measurements is obtained. Sensitivity analysis demonstrates that the AM process is significantly affected by the laser power and the feeding rate, while poorly influenced by the scanning speed.

Key words: Additive manufacturing (AM), Laser Solid Forming (LSF), In-situ measurements of residual stresses; Numerical simulation; Thermo-mechanical analysis.

1. Introduction

Laser Solid Forming (LSF) is an advanced high-efficiency additive manufacturing (AM) technology allowing for the fabrication of complex, free-shape, high-performance metal components for the aerospace industry. At the same time, LSF enables an optimized use of raw material with a considerable cost saving return [1-2]. However, the material properties of AM parts are affected by the complex layer-by-layer fabrication technique, characterized by repeated fast heating and cooling cycles, complex non-linear material behavior going through repeated phase-change transformations and cyclic annealing processes. Due to the large thermal gradients at the Heat Affected Zone (HAZ), large residual

---

stresses are generated, leading to undesired distortions, cracks and even premature failure during the AM building process or in service [3-7]. Hence, it is important to understand the thermo-mechanical behavior of the material during the manufacturing process for accurately predicting and efficiently controlling the formation of residual stresses and distortions.

Nowadays, in order to obtain high-quality components, the trial-and-error optimization process is adopted, resulting in large time and material consumption and the reduction of the cost-effectiveness of the fabrication technology. Accurate numerical simulation of the AM process makes possible to predict the thermo-mechanical behavior of the material during the layer-by-layer deposition sequence, including the temperature field [8-11], the distortions and residual stresses [12-17], as well as the microstructure evolution and the phase-change transformations [18-19].

However, the computational models typically used to study the AM process are quite limited because of the large amount of computational time required, the challenges of the experimental measurements necessary to calibrate and validate the numerical models and the lack of temperature-dependent material property data-bases to characterize the material behavior within the entire temperature range from the room temperature to (and above) the melting point [12]. Different in-situ monitored methods have been used to record the temperature field, distortions and residual stresses evolution during the metal deposition process for different AM technologies. Chiumenti *et al.* [8-9] utilized thermo-couples to measure the thermal history at different location of Ti-6Al-4V parts during the AM process. The experimental measurements were used to calibrate the in-house Finite Element (FE) software for thermo-mechanical analysis and modeling of AM processes. Seppala [20] used the infrared (IR) imaging to monitor the temperature field of polymers during thermoplastic AM. These measurements were used to develop a numerical strategy to control and simulate the AM process. Farshidianfar *et al.* [21-22] developed an IR imaging system to study the influence of the molten pool temperature and cooling rate on the microstructure evolution of 316L stainless steel components fabricated by laser AM. As a result, a novel close-loop feedback PID controller based on IR imaging system was developed to control and optimize the metal deposition strategy by a real-time monitoring of the cooling rate during AM. Yang *et al.* [23] adopted a IR camera to investigate the thermal behavior of gas metal arc welding (GMAW) of AM thin-walls under different inter-layer cooling time.

The literature survey also reports a large number of in-situ measurements as well as numerical simulations to investigate distortions and residual stresses in AM. Denlinger et al. [16-17,24-25] measured vertical displacements using Laser Displacement Sensors (LDS) and calculated both the deformations and the residual stresses of Ti-6Al-4V cantilever substrates induced by electron beam and laser in AM processes. They also investigated the vertical displacement of the substrate using a Differential Variable Reluctance Transducer (DVRT) in Selective Laser Melting (SLM). These works just perform a point-wise comparison between the numerical results and the experimental measurements. This is not enough to generate a more general understanding of the AM process. Afazov et al. [26] adopted optical 3D-scan measurements to evaluate the final distortions of blade components fabricated by SLM. They developed a FEA-based compensation method by comparing the actual distortions with the reference geometry. Yang et al. [27] measured the final deformation of the bottom surface of their substrate using a 3D laser scanner. The measurements have been used to calibrate their mechanical model.

Residual stresses can be measured either using destructive techniques such as the hole drilling [28], contour methods [29] and X-ray diffraction methods on surface [30], or non-destructive measurements including both synchrotron X-ray and neutron diffraction methods on bulk materials [31,32]. All these methods must be applied on

completely finalized AM components. Contrarily, full field, non-tactile and high-precision, digital image correlation (DIC) has been widely applied in real-time measurements during the fabrication [33]. Ocelík et al. [34] adopted the DIC technology to observe the evolution of strains at the bottom plate surface during laser cladding. Biegler [35] and Xie [36] successfully employed DIC together with optical filters (to block the intense laser light) to measure the strains field directly on the prefabricated build rather than on the substrate. Wu et al. [37] presented a destructive residual stress measurement at surface-level based on DIC observation in conjunction with build plate removal and sectioning.

In this work, an exhaustive in-situ measuring campaign is carried out to observe the evolution of different thermo-mechanical fields. Thermocouples, IR imaging, displacement sensors and DIC with optical filter are used to monitor the fabrication of LSF parts. The experimental data is used to, firstly, calibrate and, later, optimize the thermomechanical model used for the AM simulation of the LSF process. Finally, the validated model is used to predict both residual stresses and distortions.

2. Experimental campaign

2.1. Experimental setup

A series of Ti-6Al-4V powder fed multilayer single-walls coupons are built on annealed Ti-6Al-4V substrates. The substrates are 140 mm long, 6 mm wide and 25 mm thick. Each single-wall is 80 mm long built by depositing 40 layers. The energy input makes use of a YLS-3000 IPG Photonics fiber laser in a close protective casing filled with argon to prevent oxidation during the LSF process. The laser has a maximum power of 3 kW operating within 960~1200 nm wavelength range. The laser beam diameter on the plate surface is of about 3 mm and presents a Gaussian profile. Ti-6Al-4V powders are fabricated by Plasma Rotating Electrode Processed (PREPed) with a spherical particle size between 48 and 150 μm (-100/+300 sieve size). The powder is dried in a vacuum oven at 130ºC during 3 h before supplying it to the feeding device. The powder feeding into the molten pool is coaxial to the energy input and makes use of an in-house designed cladding head.

The influence of the laser power, the scanning speed and the feeding rate on thermo-mechanical quantities such as temperature evolution and residual stresses is studied. Table 1 presents these different LSF process parameters used and the corresponding final dimensions of the resulting build.

Table 1 Processing parameters of LSF process and final dimensions of each single-wall.

Case	Power input (W)	Scanning speed (mm/s)	Up-lift height (mm)	Feeding rate (g/min)	Wall height (mm)	Wall width (mm)
1	1500	10	0.55	12.0	21.6	5.0
2	1000	10	0.5	12.0	21.2	4.0
3	800	10	0.35	12.0	15.6	3.0
4	1000	10	0.3	8.0	12.8	3.8
5	1500	15	0.4	12.0	14.0	4.0
6	1000	15	0.3	12.0	14.4	3.6

2.2 In situ temperature and strain measurement

In order to measure both the temperature and the strain fields, one side of the substrate is clamped to the supporting structure, while the opposite side can freely move during the LSF process as shown in Fig. 1.

In-situ distortion is monitored with two WXXY PM11-R1-20L Displacement Sensors (DS): one located at 5 mm

from the free edge of the substrate and another one at the bottom surface of the substrate, 40 mm from the free edge, as shown in Fig. 2. This kind of DS has a measuring accuracy of 0.02% and a range of 20 mm. In addition, a commercial DIC system with optical filters was employed to measure the distortion of the entire sample during the entire duration of the LSF process. It employs two CMOS cameras for the image acquisition and a specific software for the image correlation. Stochastic high contrast pattern is used to capture and track the substrate movement. The cameras are placed to a distance of 330 mm from the metal deposition with 200 mm distance between them.

Two kinds of *in-situ* temperature measurements are provided. On the one side, the temperature evolution is measured using Omega GG-K-30 type K thermocouples at different locations on the substrate (see Fig. 2). The measuring uncertainty of these thermocouples is of 2.2ºC which corresponds to 0.75% of recording error. On the other side, the temperature is measured by IR thermal image method allowing for monitoring the temperature field of the entire deposition during the LSF process. Hence, this thermal camera is positioned close to sample and directly focusing on the deposition region. The thermal imager is calibrated to record temperatures in the range between 600-2000ºC with 2 Hz recording frequency.

Displacement sensors and thermocouple signals are recorded using a Graphtec GL-900 8 high-speed data-logger.
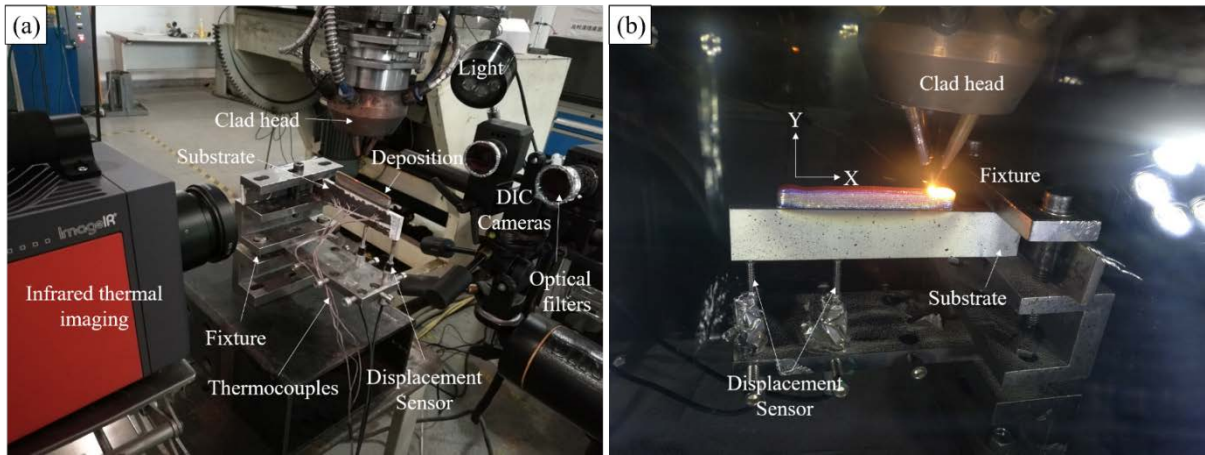

Fig. 1. Experimental setup to measure the thermomechanical field of the part during the LSF process: (a) In-situ thermo-mechanical field minitoring system, including IR thermal imaging and thermoocouples to record the temperature field, DS and DIC system to measure the mechanical field; (b) LSF processing.
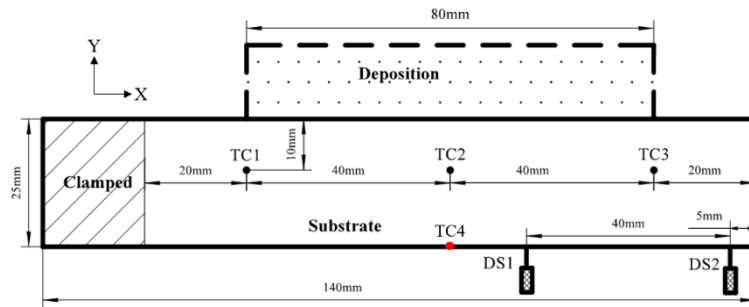

Fig. 2. Sample dimensions and location of the thermocouples and deformation sensors.

3. Numerical modeling

In this study, a fully coupled thermo-mechanical framework for the simulation of the LSF process is used. In a staggered two-stage strategy, for each time-step, firstly the transient thermal problem is solved. Next, the mechanical problem is solved for the temperature distribution obtained in the first stage. This is consistent to the fact that the AM is a

thermally driven process where both the distortions and residual stresses are caused by the temperature gradients induced at the molten pool by the laser energy input. The mechanical analysis is based on a visco-elasto/visco-plastic constitutive law including strain hardening, thermal softening and the annealing effect for temperatures close to the melting point. The detailed description of the thermo-mechanical model used has been detailed in previous publications [8,11,13,15].

3.1 Thermal analysis

The balance of energy equation governing heat transfer is:

$$\dot{H} = -\nabla \cdot \mathbf{q} + \dot{Q} + \dot{D}_{mech} \tag{1}$$

where $\dot{H}$ is the enthalpy rate, $\dot{Q}$ is the heat source into the system and $\dot{D}_{mech}$ is the thermo-mechanical dissipation. The heat source (per unit of volume) is defined as a uniform distribution of the power input effectively absorbed by the powder within the Heat Affected Volume (HAV).

The heat flux, $\mathbf{q}$, is defined by the Fourier's law:

$$\mathbf{q} = -k\nabla T \tag{2}$$

where k is the temperature-dependent thermal conductivity.

The heat loss by convection, q_{conv}, is computed through Newton's law of cooling as:

$$q_{conv} = h_{conv}(T - T_{env}) \tag{3}$$

where h_{conv} is the Heat Transfer Coefficient (HTC) by convection, T is the surface temperature of the part and T_{env} is the temperature of the surrounding air.

The heat loss by radiation is defined through Stefan-Boltzmann's law as:

$$q_{rad} = \varepsilon_{rad}\sigma_0(T^4 - T_{env}^4) \tag{4}$$

where ε_{rad} is the emissivity coefficient and σ_0 denotes Stefan-Boltzmann's constant.

3.2. Mechanical analysis

The mechanical problem is governed by the balance of momentum (equilibrium) equation expressed as:

$$\nabla \cdot \boldsymbol{\sigma} + \mathbf{b} = 0 \tag{5}$$

where $\boldsymbol{\sigma}$ is Chauchy's stress tensor and $\mathbf{b}$ denotes the body force.

The mechanical constitutive law is expressed as:

$$\boldsymbol{\sigma} = \mathbf{C} : \boldsymbol{\varepsilon}_e \tag{6}$$

where $\mathbf{C}$ denotes the fourth order constitutive tensor, and ε_e is the elastic strain computed as:

$$\boldsymbol{\varepsilon}_e = \boldsymbol{\varepsilon} - \boldsymbol{\varepsilon}_p - \boldsymbol{\varepsilon}_T \tag{7}$$

where $\boldsymbol{\varepsilon} = \nabla^s\mathbf{u}$ is the total strain tensor defined in terms of the symmetric gradient of the displacement field u, $\boldsymbol{\varepsilon}_p$ are the plastic deformations and $\boldsymbol{\varepsilon}_T$ accounts for the thermal deformation during both heating and cooling as well as the shrinkage occurring during the phase transformation. The thermo-visco-elasto-visco-plastic model suitable for the material characterization during the LSF process has been described in references [13,15]. Denlinger et al. [17] proposed that the alpha-beta phase transformation (600°C–980°C) of the Ti-6Al-4V leads to the stress relaxation of materials in AM. They set the annealing temperature to 690°C to take into account the stress annealing to achieve good agreement with the experimental evidence. However, Chen et al. [38] developed a model for EBAM in ANSYS to study the annealing temperature due to the alpha-beta phase transformation of the Ti-6Al-4V and finally fixed it to 850°C using different temperature XRD measurements. Because of the non-unique definition of the constitutive laws for the characterization of the material behavior used to simulate the mechanical response of the AM parts, the value of the annealing temperature needs to be deepened. In this work, a temperature-dependent J2 yield surface reduces according to

the temperature increase. When the material temperature is above the annealing temperature (about 750ºC), the annealing effect takes place. Hence, above the annealing temperature, the material is characterized by a pure viscous behavior and the plastic strain history as well as the strain hardening is reset.

3.3 Model description

The numerical simulations of the LSF process are carried out with the *Comet* software developed by the International Center for Numerical Methods in Engineering (CIMNE) [39]. The GiD pre-post-processor is employed to create the 3D models, generate the mesh and for the result post-processing [40].

Fig. 3 shows the 3D finite element model of the single-wall utilized for the numerical simulation of the LSF process and for its calibration through in-situ measurements. The finite element mesh consists of 15,840 Q1P0 hexahedral 8-noded elements and 21,045 nodes. The mesh size has been designed according to a convergence study as well as regarding the computational efficiency of the numerical model: 5 elements have been placed through the wall thickness and 1 per layer thickness.
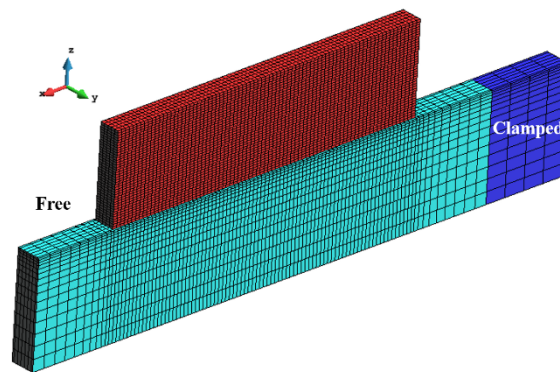

Fig. 3. FE mesh used for the numerical simulation of the LSF process.

Temperature-dependent thermal and mechanical properties of Ti-6Al-4V alloy used in the thermo-mechanical analyses are given in Table 2 [11]. The heat conductivity above the melting point has been increased to account for the heat convection flow inside the melt pool [41].

able 2 Temperature-dependent material properties of Ti-6Al-4V.

Temperature (ºC)	Density (kg/m3)	Thermal Conductivity (W/(m·ºC))	Heat Capacity (J/(kg·ºC))	Poisson's Ratio	Thermal Expansion Coefficient (μm/m/ºC)	Young's Modulus (GPa)	Elastic Limit (MPa)
20	4420	7	546	0.345	8.78	110	850
205	4395	8.75	584	0.35	10	100	630
500	4350	12.6	651	0.37	11.2	76	470
995	4282	22.7	753	0.43	12.3	15	13
1100	4267	19.3	641	0.43	12.4	5	5
1200	4252	21	660	0.43	12.42	4	1
1600	4198	25.8	732	0.43	12.5	1	0.5
1650	3886	83.5	831	0.43	12.5	0.1	0.1
2000	3818	83.5	831	0.43	12.5	0.01	0.01

Both heat convection and heat radiation conditions have been imposed at the external surfaces of both the substrate and the actual build of the single-wall according to the metal deposition process. The convection HTC during deposition

process is set to 7 W/(m^2·^{o}C), while the heat emissivity coefficient used is 0.7. The ambient temperature is set to 25°C.

The supporting structure has not been simulated. Nevertheless, the heat loss by conduction through the contact surfaces between the substrate and the metallic fixture has been accounted for by a HTC of 100 W/(m^2·^{o}C) (see Fig. 3).

The power absorption, η, has been determined by in-situ experimental calibration. The value chosen is 0.3.

4. Results and discussion

4.1. Temperature field

The temperature evolution of the substrate obtained through the numerical simulation of the LSF process is compared with measurements recorded by different thermocouples as shown in Fig. 4. These results correspond to the 6 test cases detailed in Table 1. The test cases are characterized by a variation of the process parameters in terms of scanning speed, energy input and feeding rate. The metal depositions also present some small differences in terms of final height and width of the build. In all cases, there is a remarkable agreement between the numerical predictions and the experimental measurements.
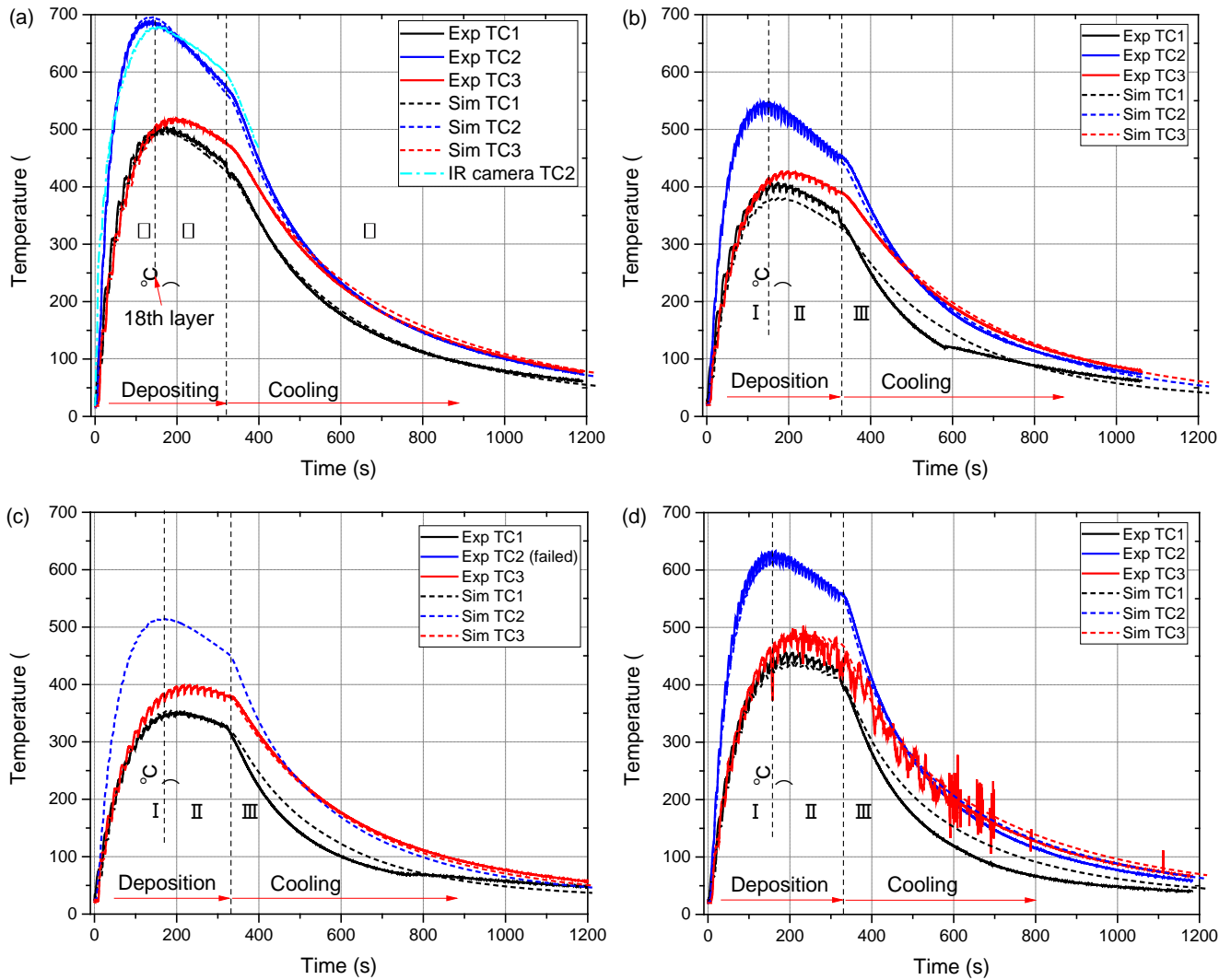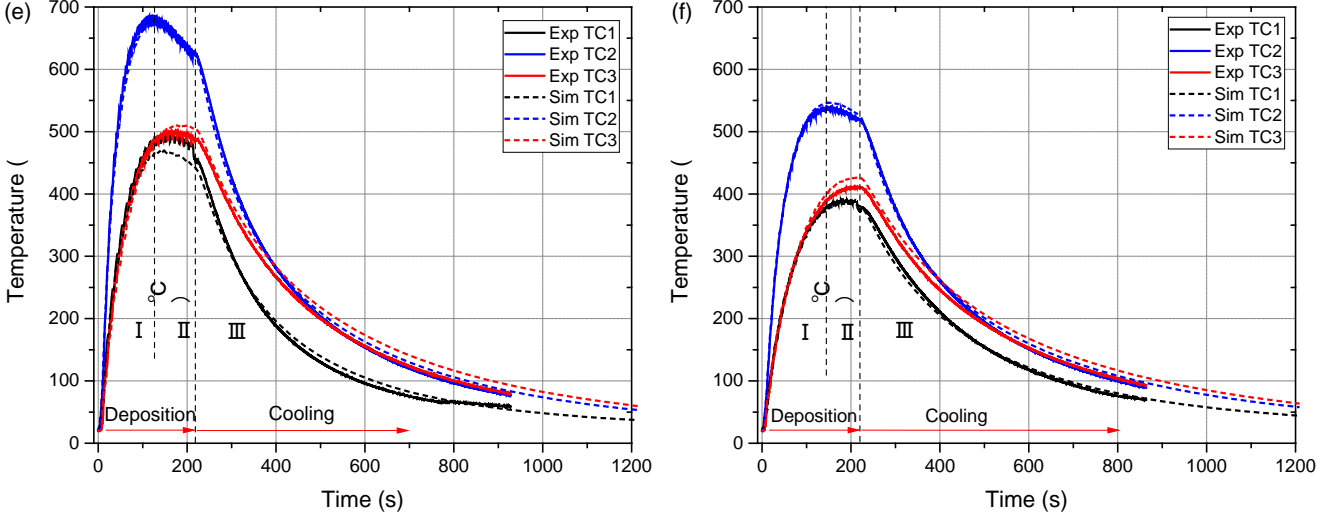
Fig. 4. Comparison between calculated and recorded thermal history at each thermocouple according to different process parameters: (a) Case 1; (b) Case 2; (c) Case 3; (d) Case 4; (e) Case 5; (f) Case 6.

The temperature curve using the Case 1 as a reference can be divided into 3 zones (see Fig. 4(a)). Firstly, the heating phase, where the temperature reaches the peak value of about 680ºC. Next, during the full duration of the metal deposition, the substrate temperature slowly reduces due to the increasing distance between the thermocouples and the actual layer. Finally, the cooling process characterized by a rapid reduction of the temperature to reach the equilibrium. Note that thermocouple TC2, located in the middle of the substrate, presents a higher temperature compared to TC1 and TC3. Although the location of thermocouples TC1 and TC3 is symmetric with respect to the center of the metal deposition, the temperature registered at TC3 is slightly higher than at TC2. The reason for this is that thermocouple TC1 is closer to the clamping system and reflects the heat dissipation by heat conduction through the supporting structure.

The average percent error is computed as:

$$\%Error = \frac{100 \sum_{i=1}^{n} \left| \frac{(x_{exp})_i - (x_{sim})_i}{(x_{exp})_i} \right|}{n} \tag{8}$$

where n is the total number time increments necessary to complete the transient simulation, i is the current time increment, x_{sim} is the temperature obtained with the simulation, x_{exp} is the corresponding experimental value. Table 3 shows the average error computed for each thermocouple. The maximum value is less than 9.47% among all test cases.

Table 3 Errors of the thermal histories at each thermocouple.

|	Case 1	Case 2	Case 3	Case 4	Case 5	Case 6
TC1	2.46	9.47	5.83	9.37	4.87	2.79
TC2	3.05	2.35	-	4.21	3.85	3.06
TC3	2.93	2.03	2.91	5.34	4.29	3.92

Fig. 5 shows the peak temperature and the final temperature after the deposition of the last layer at thermocouple TC2 for each test case. It is observed that both the peak and final temperature decrease as the laser power, P, (Case 1, 2 and 3) reduces. When the power is reduced by 33% (Case 5 vs. Case 6), the peak temperature is 20% lower. When the feeding rate is reduced by 33% (Case 2 vs. Case 4), the peak temperature is 15% higher. When the scanning speed, v, is increased by 50% (Case 1 vs. Case 5), the peak temperature keeps almost constant while the final temperature is 10% higher. Moreover, comparing Case 2 vs. Case 5, where the heat input is identical, the temperature of Case 5 is higher

than Case 2. This is due to the fact that heat dissipation does not depend on the scanning speed. Hence, by increasing the scanning speed, the heat is not evacuated faster because the heat loss depends on the HTC only. Furthermore, by increasing the scanning speed, the difference between peak and final temperatures is reduced. Therefore, both the laser power and feeding rate sensibly affect the thermal response of the build, while increasing the scanning speed has a limited effect: thanks to the quick movement of the heat source, a more uniform temperature field is favored.
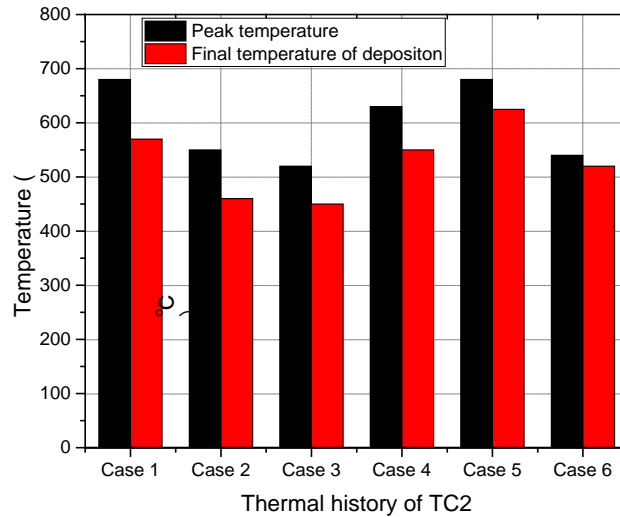
Fig. 5. Peak temperatures and final temperatures after the deposition of the last layer at thermocouple TC2 for each test case.

The use of thermocouples is also used to calibrate the IR thermography images (see Fig. 1(a) and Fig. 2). The emissivity value is the most important value to be determined to achieve the required accuracy in the determination of the temperature field. Once calibrated, the temperature profile measured by IR camera agrees with the data recorded by thermocouple (see Fig. 4(a)).

The advantage of using the IR camera consists of capturing the temperature distribution of the entire geometry of the single-wall build during the LSF process, with good reliability and accuracy. This can be compared with the temperature contour-fills obtained from the numerical simulation.

Fig. 6 shows the contour-fills of the temperature after the deposition of the 1st, 5th, 15th, 25th and 40th layer, as well as 1 s and 10 s after the beginning of the cooling phase. The pictures on the left hand side correspond to the numerical analysis while, on the right hand side, the IR images are reported.

It can be seen that when the 1st layer is deposited, the heat affected zone is restricted to the molten pool because the substrate is still cold. By increasing the number of deposited layers, the temperature distribution is more uniform. The highest temperatures are still located at the molten pool but the temperature gradients are less pronounced. The size of the molten pool increases together with the length of its queue.

When the deposition of the single-wall is completed, the temperature concentration at the molten pool quickly disappears, (in less than 1 s). The temperature drops very fast and, after 10 s of cooling, the contour-fill is quite uniform as shown by the IR images and the simulation results, respectively.
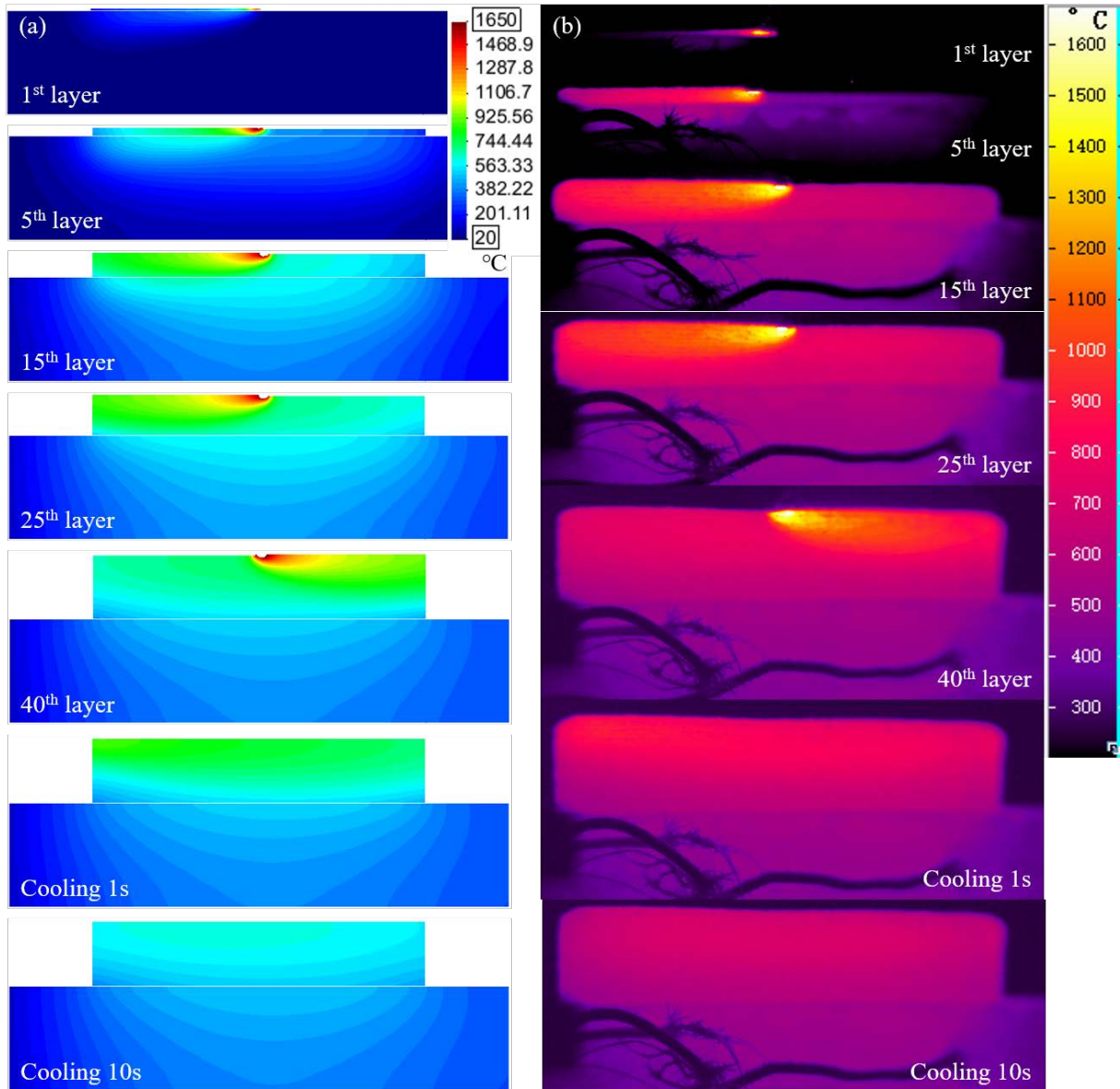
Fig. 6. The temperature field evolution of Case 3: (a) Numerical results; (b) IR measured results.

4.2. Distortion history

Fig. 7 shows the evolution of the distortion (vertical displacement) of the substrate. This figure compares the measurements recorded by the displacement sensors DS1 and DS2 and the corresponding results obtained at the same locations through the numerical simulation of the AM process. The comparison refers to the 6 test cases defined in Table 1, according to the different process parameters selected. The agreement between the numerical results and the experimental evidence is noticeable for DS2. Some discrepancies are found for DS1. One possible reason is that during the depositing process, a significant longitudinal bending of the substrate is observed. Hence, the deposition can be affected by the actual curvature of the substrate surface results. This is more evident for DS1. Note that the curvature also affects the distance between the powder feeding nozzles and the substrate, leading to a gradual increase which is proportional to the distance from the clamping. Finally, in LSF process the surface roughness generated during the deposition of the first layers can affect the stability of the process as well as the actual the layer thicknesses at

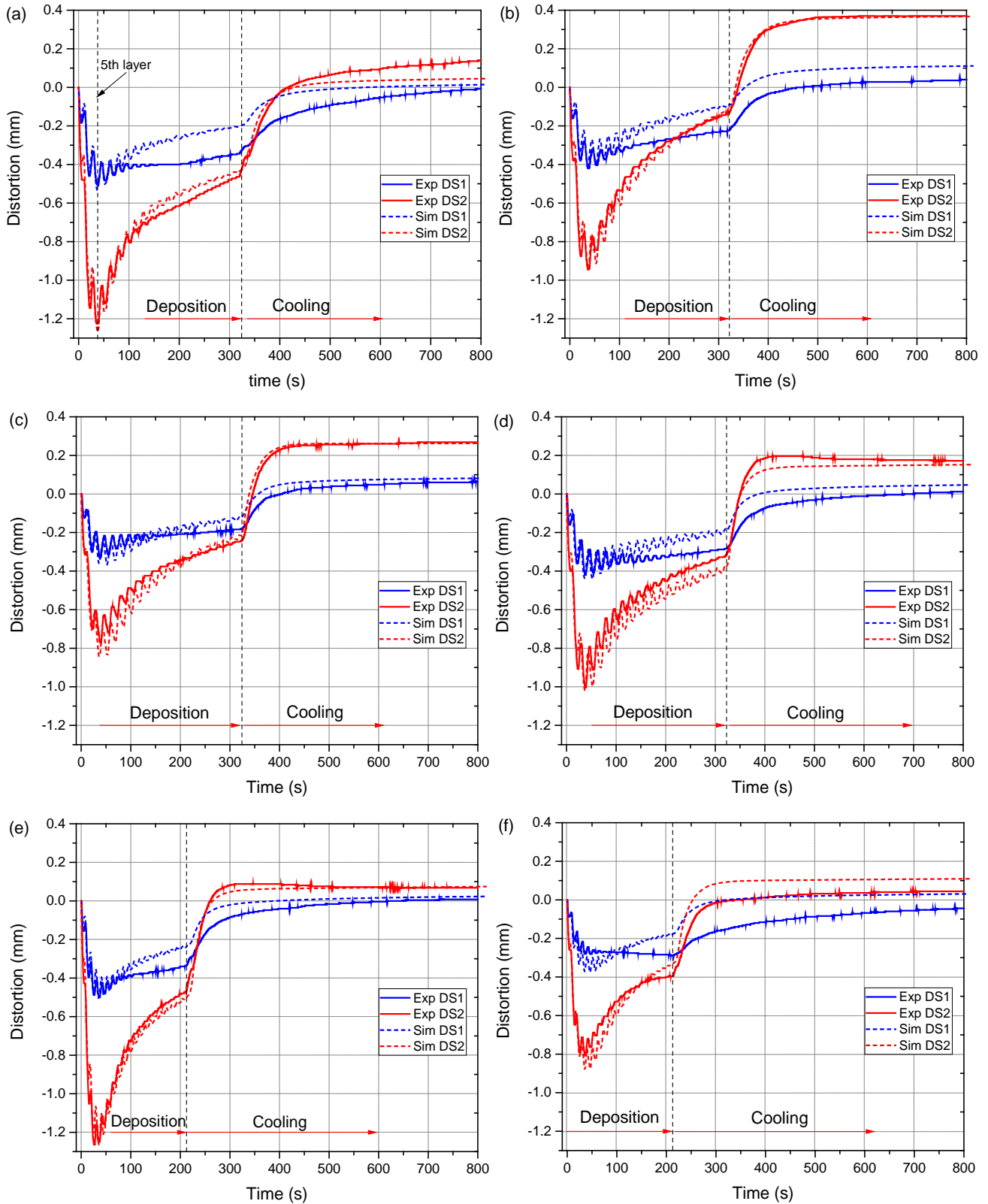different locations within the same layer.

Fig.7. Comparison between the calculated and measured distortions at each DS for different process parameters: (a) Case 1; (b) Case 2; (c) Case 3; (d) Case 4; (e) Case 5; (f) Case 6.
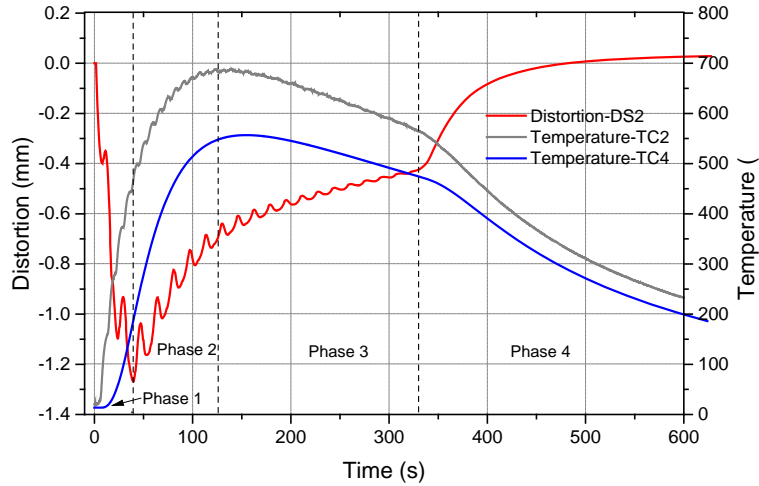
Fig. 8. Comparison between the distortion evolution of point DS2 and the calculated thermal histories of point TC2 and TC4 under Case 1 (see Fig. 2).

It can be observed that the temperature of the substrate increases sharply during the deposition of the first 5 layers (phase 1). Hence, the thermal dilatation of the upper surface of the substrate induces the fast bending of the base-plate: almost 1.25 mm downward (Case 1), which is more than the thickness of two layers deposited. During the metal deposition of the 6th to 16th layer (phase 2), the temperature still increases to reach its maximum value. Nevertheless, the distortion of the base-plate reduces due to the more uniform distribution of the temperature field and the stress release induced by the thermal softening of the material. During the deposition of the remaining layers (phase 3), both the temperature and distortion of the substrate slowly decrease. Almost 2/3 of the distortion achieved in the first phase is recovered. In the final cooling phase, the temperature of the build gradually cools down to the room temperature and the distortion tends to disappear. The residual vertical displacements are less than 0.38 mm, which is smaller than the thickness of one layer ensuring an acceptable geometrical accuracy of the fabricated component.

It can be seen from Fig. 7 that the thermo-mechanical behavior is affected by the process parameters selected. When the laser power is reduced by 47% (Case 1 vs. Case 3), the maximum vertical displacement is reduced by 37%. Reducing 33% the feeding rate (Case 2 vs. Case 4), the maximum vertical displacement is almost the same, but the residual distortion is reduced by 53%. Increasing 50% the scanning speed (Case 1 vs. Case 5), the distortion is very similar. Therefore, the mechanical response of the AM component is very sensitive to the laser power and the feeding rate, while being poorly influenced by the scanning speed.

Fig. 9 compares the vertical displacements measured by the DIC camera with the corresponding numerical results at different process times. Remarkable agreement is achieved at all stages of the process.

Fig. 10 compares the final distortions obtained from the numerical simulation with the experimental results of the single-wall under Case 1 and 2. The numerical results are amplified (×3) to highlight the substrate distortion. The maximum distortion is located near the free end of the sample and corresponds to the deposition of the 4th-6th layers. This is due to the large bending of the substrate after deposition of the first 5 layers, as previously discussed.
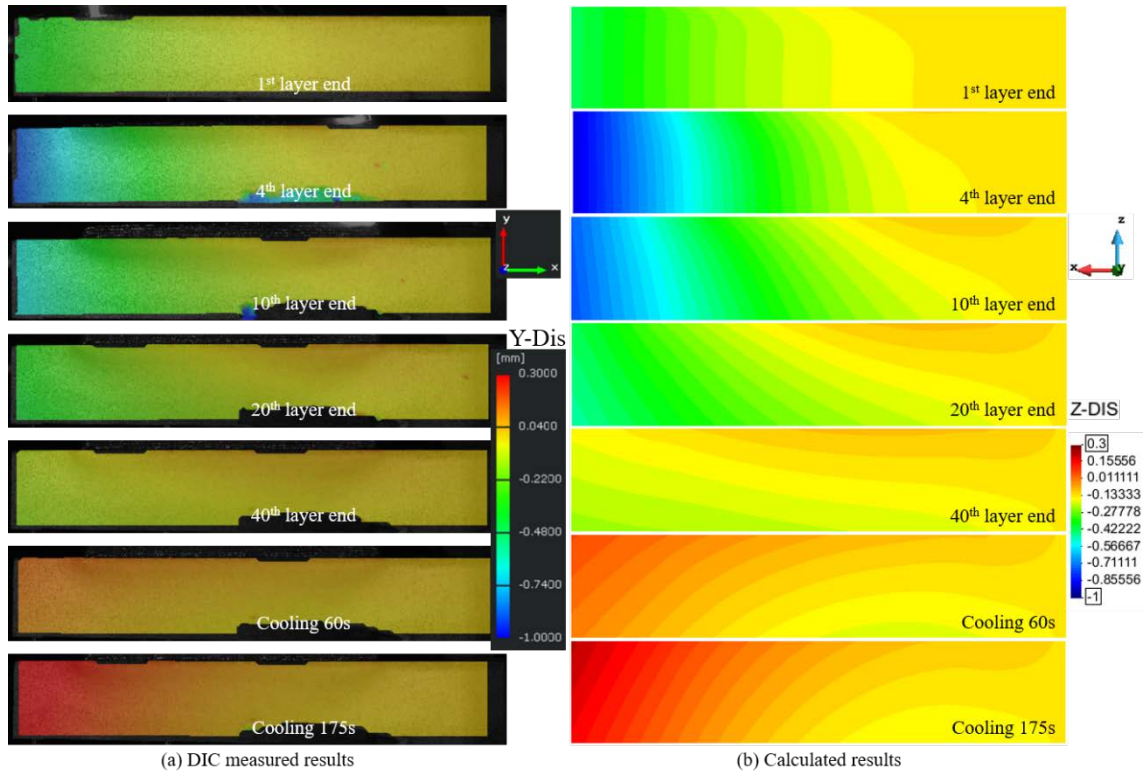
Fig.9. Comparison of the DIC measured and simulated vertical distortions at different process time.
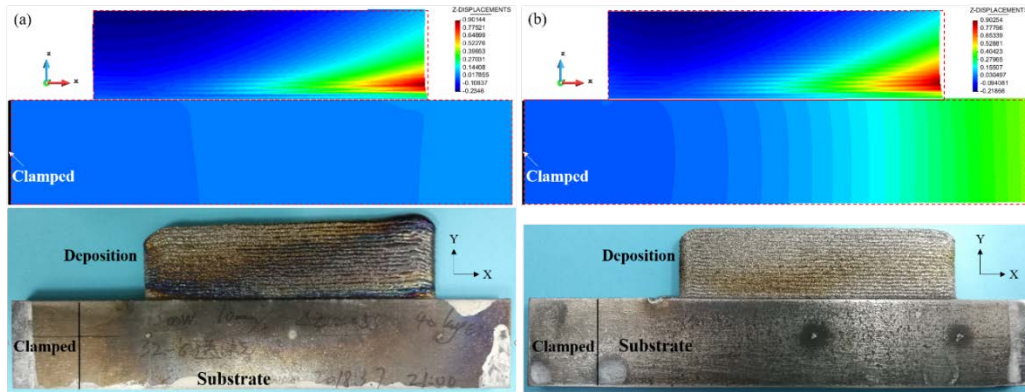

Fig. 10. Comparison between the calculated residual distortions (with magnification factor of 3) and the experimental results: (a) Case 1; (b) Case 2.

4.3. Strain field

The evolution of strain field (Case 2) obtained by DIC cameras is shown in Fig. 11. Fig. 11(a) shows the area where all DIC measurements are analyzed. Fig. 11(b) and 11(c) show the distributions of the longitudinal, ε_{xx}, and normal, ε_{yy}, strain fields, respectively. When the 1st layer is deposited, the thermal expansion induces large vertical strain close to the top surface of the substrate. Following with the deposition process, the area affected by large strains expands due to the thermal diffusion through the substrate. The maximum values recorded correspond to the deposition of the 20th layer both for the longitudinal and vertical strain fields according to the peak temperatures observed during the AM process. The largest strains are located in the central/top area of the base-plate which corresponds to the most heat affected zone.
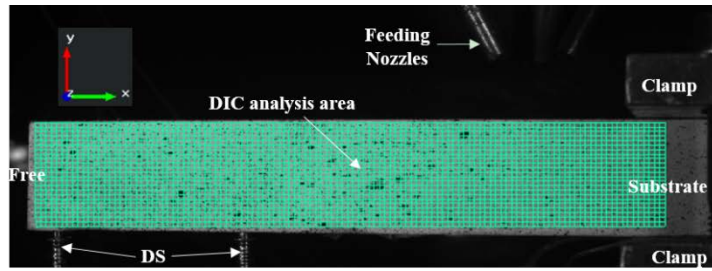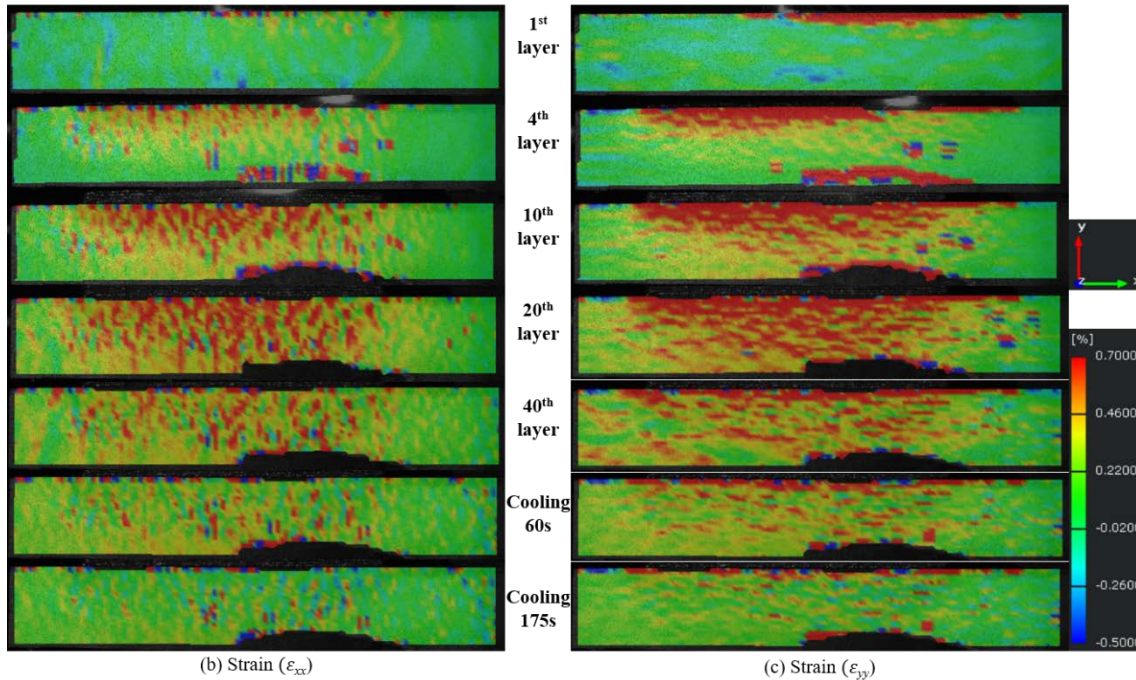
(a) Schematic of DIC analysis area

(b) Strain (ε_{xx})

(c) Strain (ε_{yy})

Fig. 11. Evolution of the strain field of the substrate recorded by DIC cameras (Case 2).

4.4. Stress field

Due to the geometry of the single-wall as well as the type of clamping system adopted, the longitudinal stresses, σ_{xx}, are the more relevant. Fig. 12 shows the evolution of the longitudinal stresses for Case 1. Large tensile stresses (up to 544 MPa) induced by the contraction of the 1st layer can be observed as well as the compressions (up to -300 MPa) in the upper side of the base-plate. Once again, this is due to the thermal shrinkage of the material located in the heat affected zone. The stress field starts reducing after the deposition of the 3rd layer due to the reduction of the thermal gradients because of the higher temperature of the substrate. The more homogenous the temperature field becomes, the lower stress level is observed. After 50 s of cooling, the residual tensile stresses are located at the end-side of the metal deposition due to the contraction of the build.

Fig. 13 shows the residual stresses (σ_{xx}) according to the different process parameters (Cases 1 to 6). It can be concluded that the resulting contour-fills are very similar, being little affected by the process parameters. Nevertheless, reducing 47% the laser power (Case 1 vs. Case 3), the maximum tensile stress is (locally) increased by 82%. This is due to the stress release induced by the phase transformation of Ti-6Al-4V titanium alloy at the higher temperatures [17]. Reducing 33% the feeding rate (Case 2 vs. Case 4), the maximum tensile stress is reduced by 26%. This is because reducing the amount of powder deposited results in the reduction of the heat needed to melt it. Hence, at the heat affected zone the peak temperature is higher, provoking higher thermal gradient and stresses. Moreover, when the scanning speed

is increased by 50% (Case 1 vs. Case 5), the residual longitudinal stresses of the part are slightly modified. Thus, the maximum residual stress of the build is mostly influenced by the laser power and feeding rate while slightly affected by the scanning speed.

In addition, the vertical distortions of the substrate are mainly influenced by the longitudinal stresses. Thus, some discrepancies between the simulated and the experimental results may result in that the predictions of the stresses field are not all matched with the experimental measurements. However, the stresses analysis overall can be credible.
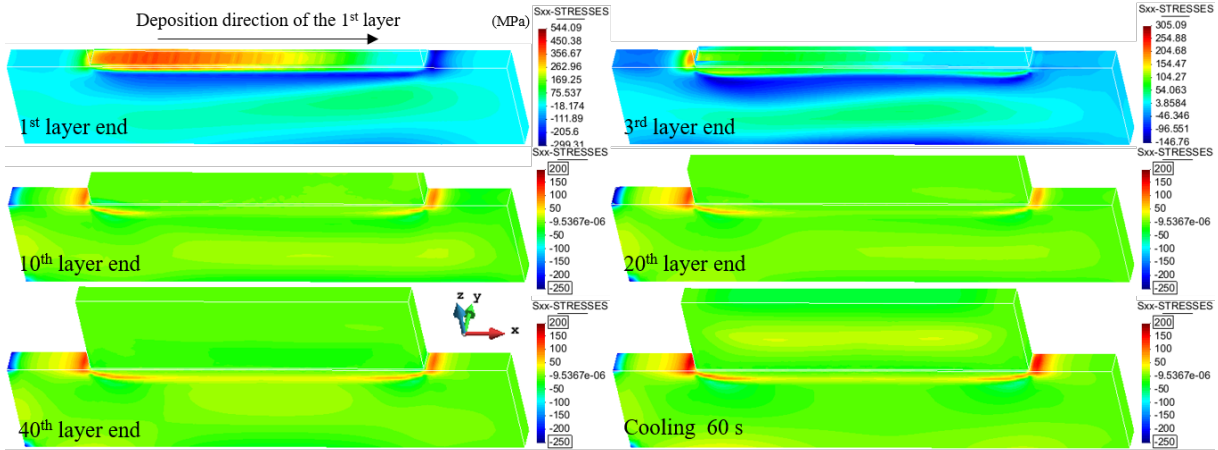

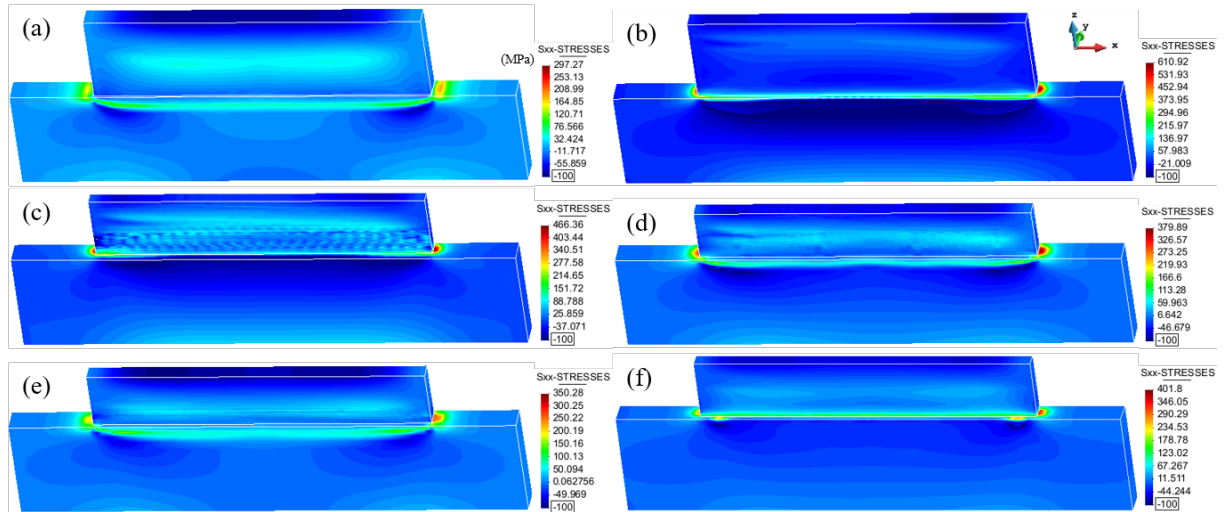Fig. 12. Evolution of the longitudinal stress (σ_{xx}) fields for Case 1.

Fig. 13. Calculated residual stresses (σ_{xx}) field for each case.

5. Conclusion

The work presented is very challenging due to the joint use of thermocouples, IR imaging, displacement sensor and DIC system to develop a systematic in-situ thermo-mechanical field measurement platform. This in-situ system is used to monitor the thermo-mechanical evolution of the Ti-6Al-4V single-walls during the LSF process. At the same time, the in-house coupled 3D thermo-mechanical software is experimentally calibrated to analyze the thermo-mechanical behavior of LSF builds.

Our main conclusions can be summarized as follows:

15

(1) The calculated temperature field results in very good agreement with the experimental evidence. The maximum average error at all thermocouples is less than 9.47%. The IR imaging can accurately monitor the surface temperature of both the deposition and base-plate during LSF process. High temperature field are recorded during the deposition of the first layers while reducing during the following depositions.

(2) The vertical displacement of the substrate first quickly increases and achieves the peak -1.25 mm in the 5th layer end, then gradually decreases in subsequent deposition stages. It is interesting to observe that the final distortion of each substrate is very small and less than 0.38 mm, which is beneficial for guaranteeing the geometrical accuracy of the fabricated parts. Although the calculated distortion generally matches the measured results, there are still some mismatches. A possible reason is the large bending of the supporting plate. This distortion affects the powder feeding system as well as the layer thickness and surface roughness. Hence, DSs far from the clamping structure have shown lower accuracy.

(3) The in-situ strain fields of Ti-6Al-4V single-walls during LSF process are successfully monitored by DIC method with optical filters and bright lights. Once again, the first layers are the responsible of the highest strains at the beginning of the metal deposition. The maximum value is reached after the deposition of the 20th layer, to slowly decrease later on. The distortions measured by the DIC system agree with the results obtained through the numerical simulation.

(4) The largest tensile stress (up to 544 MPa) is generated during the deposition of the 1st layer. With the deposition of the following layers, the stress field quickly decreases due to the thermal softening of the base-plate. The maximum longitudinal residual stresses are located at the end side of the metal deposition due to the mechanical constraint induced by the substrate. The annealing phenomena resulted to be critical for the model calibration.

(5) The thermal and mechanical responses are significantly affected by the laser power and the feeding rate while little affected by the scanning speed. However, the increase of the scanning speed favors the uniformity of the temperature field reducing the strain localizations and, consequently, the stress concentrations.

(6) Mechanical results can be enhanced by predicting the alpha/beta phase content induced by the temperature field evolution [42]. This given, the mechanical constitutive model should be coupled, not only with the temperature field but also with the metallurgical model for an improved accuracy.

6. Acknowledgements

7. References

1   Huang W, Lin X. Research Progress in Laser Solid Forming of High Performance Metallic Component[J]. Materials China, 2010(6):012-27.

2   Everton S K, Hirsch M, Stravroulakis P, et al. Review of in-situ process monitoring and in-situ metrology for metal additive manufacturing[J]. Materials & Design, 2016, 95:431-445.

3   Szost B A, Terzi S, Martina F, et al. A comparative study of additive manufacturing techniques: Residual stress and microstructural analysis of CLAD and WAAM printed Ti–6Al–4V components[J]. Materials & Design, 2016, 89: 559-567.

4   Mukherjee T, Manvatkar V, De A, et al. Mitigation of thermal distortion during additive manufacturing[J]. Scripta materialia, 2017, 127: 79-83.

5   Chen Y, Zhang K, Huang J, et al. Characterization of heat affected zone liquation cracking in laser additive manufacturing of Inconel 718[J]. Materials & Design, 2016, 90: 586-594.

6   Megahed M, Mindt H W, N'Dri N, et al. Metal additive-manufacturing process and residual stress modeling[J]. Integrating Materials and Manufacturing Innovation, 2016, 5(1): 4.

7   Wang Z, Denlinger E, Michaleris P, et al. Residual stress mapping in Inconel 625 fabricated through additive manufacturing: Method for neutron diffraction measurements to validate thermomechanical model predictions[J]. Materials & Design, 2017, 113: 169-177.

8   Chiumenti M, Lin X, Cervera M, et al. Numerical simulation and experimental calibration of Additive Manufacturing by blown powder technology. Part I: thermal analysis[J]. Rapid Prototyping Journal, 2017, 23(2): 448-463.

9   Shen N, Chou K. Thermal Modeling of Electron Beam Additive Manufacturing Process. Powder Sintering Effects[J]. ASME Paper No. MSEC2012-7253, 2012.

10   Jamshidinia M. Numerical Modeling of Heat Distribution in the Electron Beam Melting of Ti-6Al-4V[J]. Journal of Manufacturing Science & Engineering, 2013, 135(6):61010-61011.

11   Chiumenti M, Neiva E, Salsi E, et al. Numerical modelling and experimental validation in Selective Laser Melting[J]. Additive manufacturing, 2017: 171-185.

12   Lindgren L E, Lundbäck A, Fisk M, et al. Simulation of additive manufacturing using coupled constitutive and microstructure models[J]. Additive Manufacturing, 2016, 12: 144-158.

13   Lu X, Lin X, Chiumenti M, et al. Finite element analysis and experimental validation of the thermomechanical behavior in laser solid forming of Ti-6Al-4V[J]. Additive Manufacturing, 2018, 21: 30-40.

14   Andrés A, Fachinotti V D, Gustavo E, et al. Computational modelling of shaped metal deposition[J]. International Journal for Numerical Methods in Engineering, 2011, 85(1):84-106.

15   Chiumenti M, Cervera M, Salmi A, et al. Finite element modeling of multi-pass welding and shaped metal deposition processes[J]. Computer Methods in Applied Mechanics & Engineering, 2010, 199(37–40):2343-2359.

16   Denlinger E R, Heigel J C, Michaleris P. Residual stress and distortion modeling of electron beam direct manufacturing Ti-6Al-4V[J]. Proceedings of the Institution of Mechanical Engineers, Part B: Journal of Engineering Manufacture, 2015, 229(10): 1803-1813.

17   Denlinger E R, Michaleris P. Effect of stress release on distortion in additive manufacturing process modeling[J]. Additive Manufacturing, 2016, 12: 51-59.

18   Lu L X, Sridhar N, Zhang Y W. Phase field simulation of powder bed-based additive manufacturing[J]. Acta Materialia, 2018, 144: 801-809.

19   Sahoo S, Chou K. Phase-field simulation of microstructure evolution of Ti–6Al–4V in electron beam additive manufacturing process[J]. Additive manufacturing, 2016, 9: 14-24.

20   Seppala J E, Migler K D. Infrared thermography of welding zones produced by polymer extrusion additive manufacturing[J]. Additive Manufacturing, 2016, 12(Pt A):71-76.

21   Farshidianfar M H, Khajepour A, Gerlich A. Real-time control of microstructure in laser additive manufacturing[J]. International Journal of Advanced Manufacturing Technology, 2016, 82(5-8):1173-1186.

22   Farshidianfar M H, Khajepour A, Gerlich A P. Effect of real-time cooling rate on microstructure in Laser Additive Manufacturing[J]. Journal of Materials Processing Technology, 2016, 231:468-478.

23   Yang D, Wang G, Zhang G. Thermal analysis for single-pass multi-layer GMAW based additive manufacturing using infrared thermography[J]. Journal of Materials Processing Technology, 2017, 244: 215-224.

24   Denlinger E R, Heigel J C, Michaleris P, et al. Effect of inter-layer dwell time on distortion and residual stress in additive manufacturing of titanium and nickel alloys[J]. Journal of Materials Processing Technology, 2015, 215: 123-131.

25   Dunbar A J, Denlinger E R, Gouge M F, et al. Comparisons of laser powder bed fusion additive manufacturing builds through experimental in situ distortion and temperature measurements[J]. Additive Manufacturing, 2017, 15: 57-65.

26　Afazov S, Denmark W A D, Toralles B L, et al. Distortion prediction and compensation in selective laser melting[J]. Additive Manufacturing, 2017, 17: 15-22.

27　Yang Q, Zhang P, Cheng L, et al. Finite element modeling and validation of thermomechanical behavior of Ti-6Al-4V in directed energy deposition additive manufacturing[J]. Additive Manufacturing, 2016, 12: 169-177.

28　Casavola C, Campanelli S L, Pappalettere C. Preliminary investigation on distribution of residual stress generated by the selective laser melting process[J]. The Journal of Strain Analysis for Engineering Design, 2009, 44(1): 93-104.

29　Vrancken B, Cain V, Knutsen R, et al. Residual stress via the contour method in compact tension specimens produced via selective laser melting[J]. Scripta Materialia, 2014, 87: 29-32.

30　Yadroitsev I, Yadroitsava I. Evaluation of residual stress in stainless steel 316L and Ti6Al4V samples produced by selective laser melting[J]. Virtual and Physical Prototyping, 2015, 10(2): 67-76.

31　Mishurova T, Artzt K, Cabeza S, et al. Subsurface residual stress analysis in Ti-6Al-4V additive manufactured parts by synchrotron x-ray diffraction[J]. 2018.

32　Cao J, Gharghouri M A, Nash P, et al. Finite-element analysis and experimental validation of thermal residual stress and distortion in electron beam additive manufactured Ti-6Al-4V build plates[J]. Journal of Materials Processing Technology, 2016: 409-419.

33　Pan B, Qian K, Xie H, et al. Two-dimensional digital image correlation for in-plane displacement and strain measurement: a review[J]. Measurement science and technology, 2009, 20(6): 062001.

34　Ocelík V, Bosgra J, de Hosson J T M. In-situ strain observation in high power laser cladding[J]. Surface and coatings technology, 2009, 203(20-21): 3189-3196.

35　Biegler M, Graf B, Rethmeier M. In-situ distortions in LMD additive manufacturing walls can be measured with digital image correlation and predicted using numerical simulations[J]. Additive Manufacturing, 2018, 20: 101-110.

36　Xie R, Zhao Y, Chen G, et al. The full-field strain distribution and the evolution behavior during additive manufacturing through in-situ observation[J]. Materials & Design, 2018, 150: 49-54.

37　Wu A S, Brown D W, Kumar M, et al. An experimental investigation into additive manufacturing-induced residual stresses in 316L stainless steel[J]. Metallurgical and Materials Transactions A, 2014, 45(13): 6260-6270.

38　Chen Z, Ye H, Xu H. Distortion control in a wire-fed electron-beam thin-walled Ti-6Al-4V freeform[J]. Journal of Materials Processing Technology, 2018, 258: 286-295.

39　Cervera M, Agelet de Saracibar C, Chiumenti M, COMET: Coupled mechanical and thermal analysis. Data input manual, version 5.0, technical report IT-308, (2002). http://www.cimne.upc.edu.

40　GiD: the Personal Pre and Post-Processor (2002) CIMNE, Technical University of Catalonia, http://gid.cimne.upc.edu

41　Fallah V, Alimardani M, Corbin S F, et al. Temporal development of melt-pool morphology and clad geometry in laser powder deposition[J]. Computational Materials Science, 2011, 50(7):0-2134.

42　E. Salsi, M. Chiumenti and M. Cervera, Modeling of microstructure evolution in Additive Manufacturing processes of Ti-6Al-4V, Metals - Open Access Metallurgy Journal, (2018) 8, 633, https://doi.org/10.3390/met8080633.